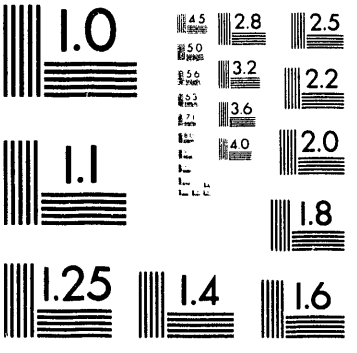
1.0
1.1
1.25
1.4
1.6
1.8
2.0
2.2
2.5
2.8
3.2
3.6
4.0
4.5
5.0
5.6
6.3
7.1

1 of 1

SANDIA REPORT

SAND92—1832 • UC—704
Unlimited Release
Printed July 1993

7613 Document Processing for
DOE/OSTI (2)

8/26/93

Shock Compression Properties of Silicon Carbide

D. E. Grady, M. E. Kipp

Prepared by
Sandia National Laboratories
Albuquerque, New Mexico 37185 and Livermore, California 94550
for the United States Department of Energy
under Contract DE-AC04-76DP00789

Issued by Sandia National Laboratories, operated for the United States Department of Energy by Sandia Corporation.

Printed in the United States of America. This report has been reproduced directly from the best available copy.

Available to DOE and DOE contractors from
Office of Scientific and Technical Information
PO Box 62
Oak Ridge, TN 37831

Prices available from (615) 576-8401, FTS 626-8401

Available to the public from
National Technical Information Service
US Department of Commerce
5285 Port Royal Rd
Springfield, VA 22161

NTIS price codes
Printed copy: A03
Microfiche copy: A01

SAND92-1832
Unlimited Release
Printed July 1993

Distribution
Category UC-704

Shock Compression Properties of Silicon Carbide

D. E. Grady
Experimental Impact Physics Department 1433
and
M. E. Kipp
Computational Physics & Mechanics Department 1432

Sandia National Laboratories
Albuquerque, NM 87185

Abstract

An investigation of the shock compression and release properties of silicon carbide ceramic has been performed. A series of planar impact experiments has been completed in which stationary target discs of ceramic were struck by plates of either similar ceramic or other appropriate material at velocities up to 2.2 km/s with a propellant gun facility. The particle velocity history at the interface between the back of the target ceramic and a lithium-fluoride window material was measured with laser velocity interferometry (VISAR). Impact stresses achieved in these experiments range between about 10 and 50 GPa. Numerical solutions and analytic methods were used to determine the dynamic compression and release stress-strain behavior of the ceramic. Further analysis of the data was performed to determine dynamic strength and compressibility properties of silicon carbide.

Sponsored by the U.S. Department of Energy and conducted under the auspices of the U. S. Department of Energy under Contract DE-AC04-76DP00789.

(Intentionally Left Blank)

Contents

Figures

Tables

Summary

The dynamic high-pressure equation-of-state and strength properties of a near theoretical density silicon-carbide ceramic were investigated through controlled planar impact and release-wave experiments. Four planar impact experiments have been completed in which stationary target discs of ceramic were struck by plates of either similar ceramic or tantalum launched at velocities up to 2.1 km/s with a propellant gun facility. One further impact experiment was performed in which a layered-impactor configuration led to multiple compression and release of the silicon-carbide sample. Impact stresses achieved in these experiments ranged between about 10 and 50 GPa. High-resolution velocity interferometer diagnostics were used to measure time-resolved transmitted particle-velocity profiles. Dynamic material properties were determined through analytic and computational evaluation of the wave profile data.

The Hugoniot of silicon carbide was determined up to an impact stress of 50 GPa. The measured Hugoniot elastic limit for this ceramic was 15.3 ± 0.4 GPa. Positive ramping of the wave behind the elastic precursor indicated increasing pressure or inelastic strain hardening with increasing deformation. A dynamic hardening behavior is also supported by increased shear strength at the Hugoniot state calculated from the difference between the dynamic uniaxial strain and hydrodynamic stress states. Analysis of elastic compressibility properties at the Hugoniot states from the release-wave data also gave results consistent with a hardening elastic-plastic behavior in silicon carbide ceramic. No clear indication of a pressure-induced phase transition in silicon carbide below 50 GPa was provided by the wave-profile data. A spall strength of approximately 0.4 GPa was determined from one experiment in which the peak stress state was about 75% of the Hugoniot elastic limit. Computational simulations of measured wave profiles in silicon carbide, including multiple shock and release, are adequately described with an elastic-plastic work-hardening model.

(Intentionally Left Blank)

1. Introduction

The present report documents recent shock compression and release data obtained on near theoretical density monolithic α-silicon carbide ceramic. The results are part of a broader study of the dynamic strength and equation-of-state properties of a range of high-strength ceramics. Earlier data and analysis are presented in Kipp and Grady (1989) and Grady (1991).

Little previous shock-wave data exists for silicon carbide. The seminal study on this material was performed by Gust, et al. (1973) more than two decades ago. In that study, shock waves in silicon carbide induced by explosive-driven flyer plates were diagnosed by monitoring free-surface displacement using inclined-mirror streak-photography techniques. A Hugoniot elastic limit of about 8 GPa was determined in that work. Hugoniot data were acquired up to a maximum shock pressure of about 100 GPa. A shock-induced phase transformation at a pressure of about 24 GPa was inferred from the data by the authors. They suggested that this transition might well be related to the known transformation in silicon.

Recently, Aleksandrov et al. (1990) have performed static high-pressure studies on silicon carbide to nearly 50 GPa. They provided initial bulk modulus and pressure derivative data. Volume dependence of the Gruneisen parameter was also established. These authors also suggested that the high pressure properties of silicon carbide are similar to those of silicon. A pressure-induced phase transformation in silicon carbide was not mentioned in the study of Aleksandrov, et al. (1990). Bassett and Weathers (see Holmquist (1991)) have also reported static compressibility data for silicon carbide to nearly 100 GPa using diamond anvil technology.

In the present study controlled impact shock- and release-wave experiments have been performed on silicon carbide. In one test partial release followed by shock recompression and release was accomplished in the silicon carbide sample. Peak stress achieved in the highest amplitude experiments was nearly 50 GPa. The lowest amplitude experiment achieved a peak stress below the Hugoniot elastic limit of silicon carbide. Hugoniot, equation-of-state, and dynamic-strength properties were determined for silicon carbide through both analytical and computational analysis of the data. A spall strength for silicon carbide ceramic was also determined from the lowest amplitude experiment.

(Intentionally Left Blank)

2. Materials

The silicon carbide tested in the current study was produced by Eagle-Picher Industries. Crystal structure of the starting material was hexagonal (alpha). The initial density and ultrasonic properties were also measured for the present material. They are: initial density = 3177 kg/m^3, longitudinal velocity = 12.06 km/s, and shear velocity = 7.67 km/s. Associated elastic properties derived from these velocities are a Poisson's ratio of $\nu = 0.16$ and $C_0 = 8.19$. Electron probe microanalysis (EPMA) revealed inclusions principally of tungsten and tungsten carbide. Minor amounts of molybdenum, chromium and titanium were also present. An equiaxial grain structure with nominal grain size of about 10 μm was determined. Porosity (about 1%) in the form of near-spherical cavities on grain boundaries was also observed. Microstructure of the starting material was adequately revealed by the back scatter EPMA image shown in Figure 1.

The lithium fluoride used as the laser window material in the present impact experiments was optically clear [100] oriented single crystals. Closed cell polyurethane foam of nominally 20 and 40 pounds per cubic foot (320 and 640 kg/m^3) provided backing material for the impactor plate. Three nines pure commercial tantalum was used as impactor material in the highest shock pressure experiment.

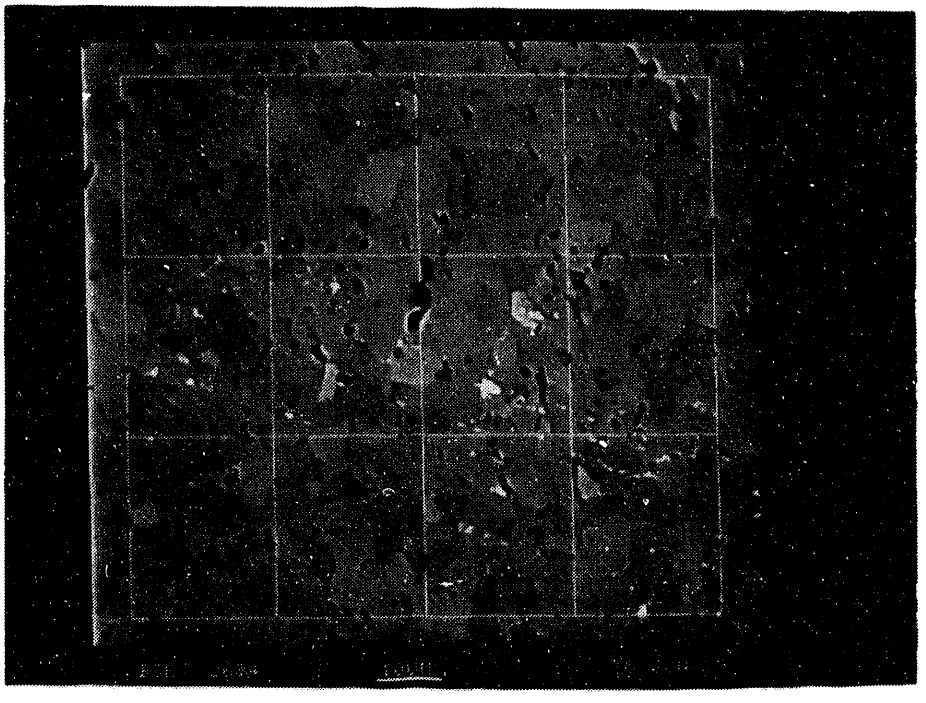

Figure 1. Back-scatter electron-probe microanalysis (EPMA) photograph of silicon carbide test material.

(Intentionally Left Blank)

3. Experimental Method

Uniaxial-strain compressive shock and release waves were produced in the monolithic silicon carbide with a single-stage powder-gun facility. The 89-mm diameter smooth-bore gun is capable of achieving a maximum impact velocity slightly above 2.3 km/s. Three electrically shorting pins were used to measure the velocity of the projectile at impact. Four similar pins were mounted flush to the impact plane and used to monitor the planarity of impact. The pins were also used to trigger diagnostic equipment: the interferometer laser, various recording oscilloscopes and transient digitizers. Projectile velocity could be measured with an accuracy of ~0.5% and the deviation from planarity of impact was typically about 10^{-3} radians.

A typical experimental configuration for the series of tests is shown in Figure 2. A disc of the ceramic being tested is mounted in the projectile and is supported on the main projectile body by a disc of low density polyurethane foam approximately 7 mm in thickness. Both 20 and 40 pounds per cubic foot (320 and 640 kg/m^3) foam were used in the present study. An aluminum ring encloses the ceramic disc as shown and provides a coplanar impact surface for electrically shorting the various diagnostic pins. For the highest impact stress experiment a tantalum plate replaced the ceramic plate in the projectile. In the partial release and recompression experiment the impacting disc was lithium fluoride approximately 3.3 mm in thickness backed by a 1.5 mm tantalum disc.

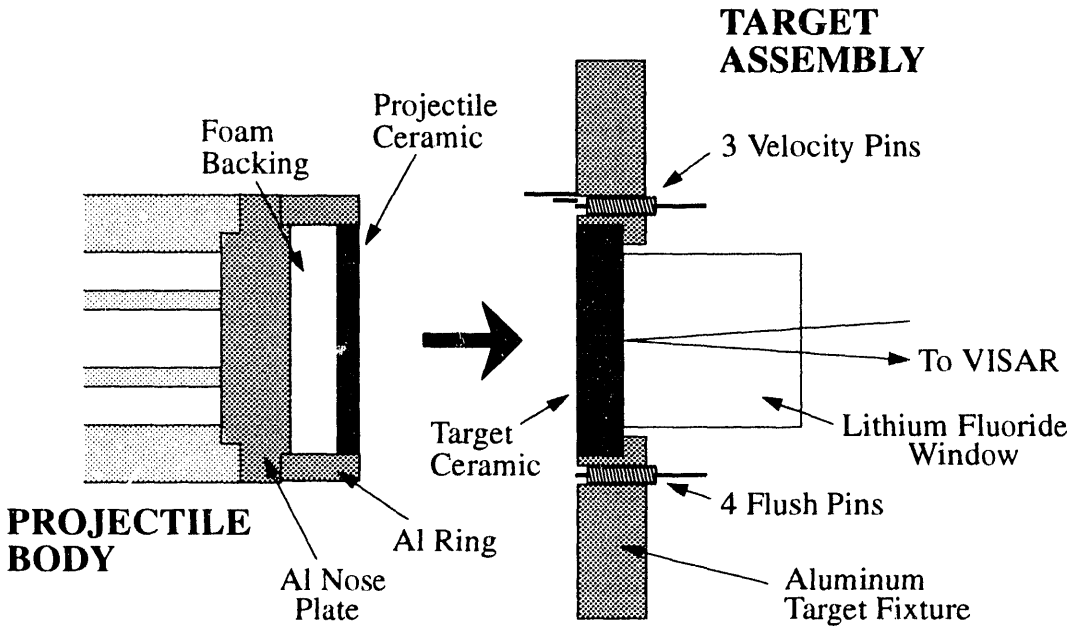

Figure 2. Experimental configuration for shock and release experiments on silicon carbide.

For the target, a disc of the ceramic was mounted in the stationary supporting target fixture. An optical quality disc of single crystal lithium fluoride was intimately bonded with epoxy to the back of this ceramic sample. All critical surfaces were lapped and polished, and were typically flat to within a few bands of sodium light. The bonded lithium fluoride surface was first lightly diffused and vapor-deposited with about 100 nm of aluminum. The ceramic-lithium fluoride epoxy-bond thickness was approximately 10 to 20 μm.

The ceramic-on-ceramic planar impact produced a compressive wave of uniaxial strain which propagated across the stationary ceramic specimen and through the ceramic-lithium fluoride interface. An equivalent compressive wave propagated through the projectile ceramic specimen and reflected at the low-impedance foam interface as a release wave which unloaded the compressed ceramic. Dimensions of the ceramic discs were selected such that lateral release waves from the boundaries of the disc did not interfere with the central motion until after the experimental measurement was completed. Similar motions were induced when a tantalum impact plate was used. In the ceramic-on-ceramic impacts the release wave traveled uninterrupted through the impact interface whereas, in the tantalum impactor case, additional wave interactions occurred at the tantalum-ceramic interface.

The compression- and release-wave behavior was measured by monitoring the time-resolved longitudinal motion at the center of the ceramic-lithium fluoride interface with laser velocity-interferometry (VISAR) techniques [Barker and Hollenbach, 1972]. Measurements were recorded on transient digitizers with a sampling period of 0.742 ns per data point. Lithium fluoride was used as the laser window material because, although its mechanical impedance is somewhat lower than the ceramic being tested, it is the only material which has been optically calibrated and which remains transparent when subjected to the 10 to 50 GPa shock stresses generated in the present experiments [Wise and Chhabildas, 1986].

The interference fringes measured with the VISAR system were converted to a time-resolved history of the velocity of the interface using the method of Barker and Hollenbach (1972), with a time resolution of approximately 1 ns. The amplitude resolution is approximately 2% of one fringe. Typically two to three fringes are achieved in the interface acceleration through the compressive shock front. From these records the dynamic stress and strain characteristics of the ceramics were determined through further computational and analytic techniques described in a later section.

A total of five shock compression experiments were performed on silicon carbide. The lowest impact velocity achieved a Hugoniot state below the Hugoniot elastic limit and provided useful nonlinear elastic and spall properties of the ceramic. The remaining experiments ranged up to Hugoniot states of approximately 50 GPa which is about three times the Hugoniot elastic limit for this material. The impact velocities and experimental dimensions for the series of experiments are provided in Table 1.

In all tests lithium fluoride windows 25.4 mm in thickness and 50.8 mm in diameter were used. The silicon carbide discs were approximately 50 mm in diameter. Note that a tantalum impactor (88 mm in diameter) was used to achieve the highest impact stress in

Table 1:
Experimental Conditions for Silicon Carbide Impact Tests

Test Number	Target Material	Impactor Material	Foam Density	Impact Velocity	Target Thickness	Impactor Thickness
			(kg/m^3)	(km/s)	(mm)	(mm)
CE-4	SiC	SiC	320	1.542	8.939	3.987
CE-5	SiC	SiC	640	2.100	8.940	3.995
CE-31	SiC	Ta	640	2.118	8.956	1.516
CE-32	SiC	SiC	320	0.612	9.841	4.958
CE-42	SiC	LiF+Ta[a]	—	2.206	4.963	3.297+1.51[a]
[a] Layered impactor — lithium fluoride backed by tantalum.						

Test CE-31. A layered lithium fluoride and tantalum impactor was used in test CE-42 to achieve specific partial release and recompression states in the silicon carbide.

One profile of the measured interface velocity is shown in Figure 3 to illustrate the nature of the compression- and release-wave data. Profiles for all tests are provided in the Appendix. The compression profile reveals the elastic-plastic wave-profile character of the

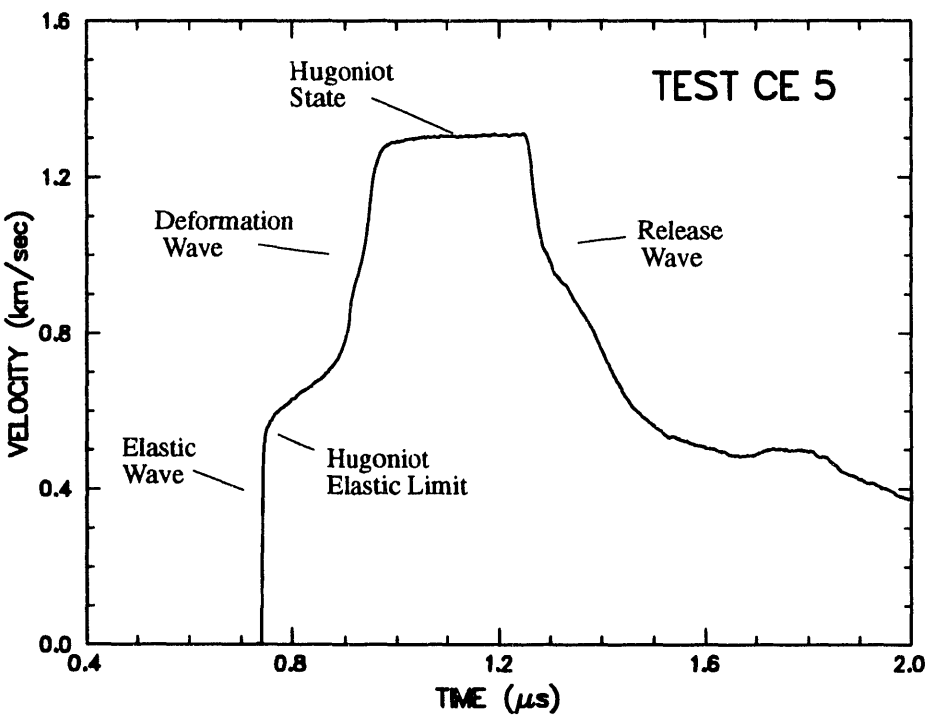

Figure 3. Silicon carbide interface velocity profile for Test CE-5.

uniaxial deformation process. The second small wavelet at about 0.9 km/s in the compressive profile between the elastic and plastic waves has been shown from computer solutions to be a consequence of a reflection at the ceramic-window interface due to the mechanical impedance mismatch and is not a material-property feature. Elastic and deformation characteristics upon release from the Hugoniot state were provided by the unloading portion of the profile in Figure 3. Late-time behavior (greater than about 2 μs) is not meaningful because lateral release waves from the sample edges can be expected to compromise the uniaxial nature of the motion.

4. Hugoniot Properties

The wave-profile data shown in Figure 3 and provided in the Appendix can be used to determine the Hugoniot properties of the silicon carbide ceramic. Here, Hugoniot states refer to the peak stress-volume-particle-velocity states achieved in the shock-compression process, recognizing that nonsteady-wave characteristics may compromise this definition. Analysis of the Hugoniot states were accomplished in several ways. In one method distinct elastic and plastic waves were first identified in the compressive profiles. By assuming steady-wave behavior, shock-wave velocities and particle-velocity increments were determined for both waves. Hugoniot relations, accounting for impedance mismatch at the recording interface, were then used to calculate the Hugoniot states. This method gave resultd in accord with Hugoniot properties determined from interface or free-surface measurements of earlier workers [e.g., Gust, et al., 1973].

Table 2:
Hugoniot Data for Silicon Carbide

	------- Elastic State -------				------- Plastic State -------			
Test Number	Shock Velocity	Particle Velocity	Stress	Specific Volume	Shock Velocity	Particle Velocity	Stress	Specific Volume
	(km/s)	(km/s)	(GPa)	(m^3/Mg)	(km/s)	(km/s)	(GPa)	(m^3/Mg)
CE-4	12.50*	0.397	15.77	0.3048	9.43	0.771	27.61	0.2928
CE-5	12.50*	0.383	15.20	0.3051	9.63	1.050	36.34	0.2839
CE-31	12.50*	0.376	14.91	0.3053	10.03	1.422	48.78	0.2729
CE-32	12.29*	0.306	11.95	0.3069	—	—	—	—

*Elastic shock velocity is calculated (see text).

Hugoniot states determined by this analytic method are provided in Figure 4 and Table 2. In the present experiments a measurement of the elastic precursor wave velocity was not made. The precursor wave velocity provided in Table 2 was estimated from the measured longitudinal ultrasonic velocity corrected for elastic nonlinearity to the Hugoniot elastic limit state by assuming a linear shock-velocity versus particle-velocity behavior ($U_s = C_l + S_l u_p$) with $S_l = 1$ (consistent with the slope of high-pressure shock- versus particle-velocity data for silicon carbide). Further computational analysis on the nonlinear elastic shock and release profile provided by experiment CE-32 supports this estimate [Kipp and Grady, 1992].

The Hugoniot elastic limit states plotted in Figure 4 and provided in Table 2 correspond to the particle velocity amplitude of the initial breakover of the elastic shock in the measured wave profile. This initial yield state does not include the subsequent pressure hardening or ramp up observed immediately behind the precursor shock which would lead to a slightly higher particle velocity level. In determining the amplitude of the particle velocity jump through the plastic wave, a more central value for the first wave amplitude was determined from the data.

The compression and release stress-volume behavior of the material was also determined with computational methods [Kipp and Grady, 1989]. With these methods a one-dimensional wave code, WONDY (Kipp and Lawrence, 1982), in conjunction with an empirical constitutive model for the ceramic was used iteratively to determine the stress-volume characteristics. Material parameters used in the calculations are listed in Table 3. Parameters in the model were adjusted until agreement with the measured velocity profile was achieved. The corresponding stress-volume behavior determined in the calculation was then accepted as the dynamic material response. Stress-volume paths determined by this method are shown in Figure 4. The peak stress states agree well with the previous Hugoniot analysis and are provided in Table 4.

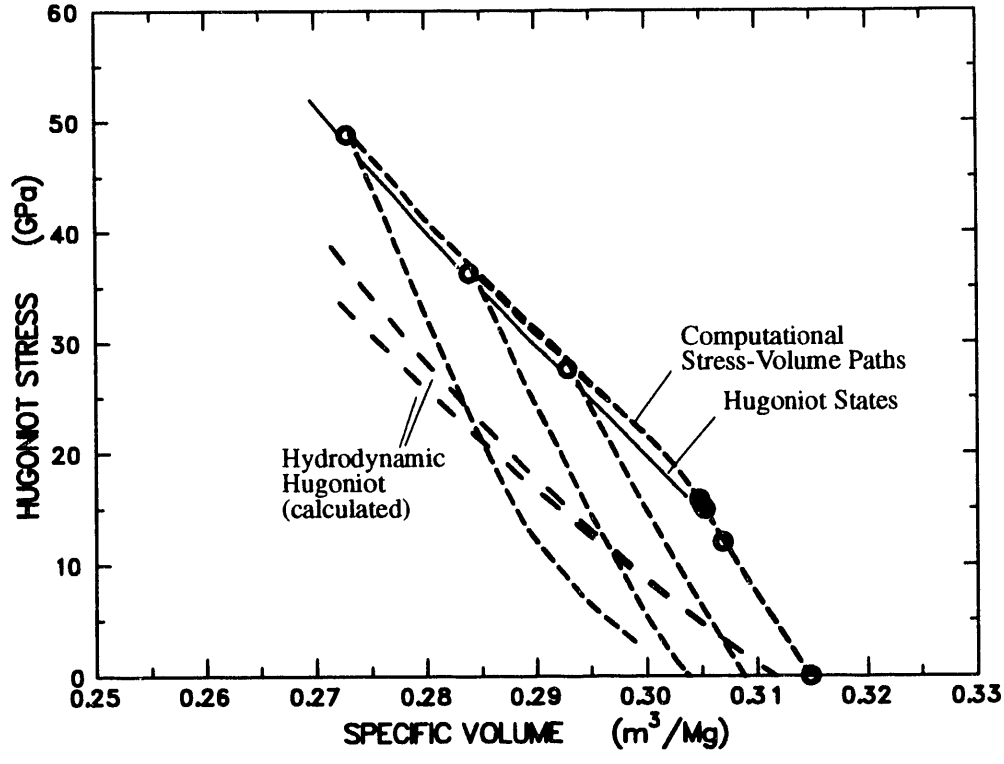

Figure 4. Hugoniot states and dynamic stress-volume paths calculated from wave profile data.

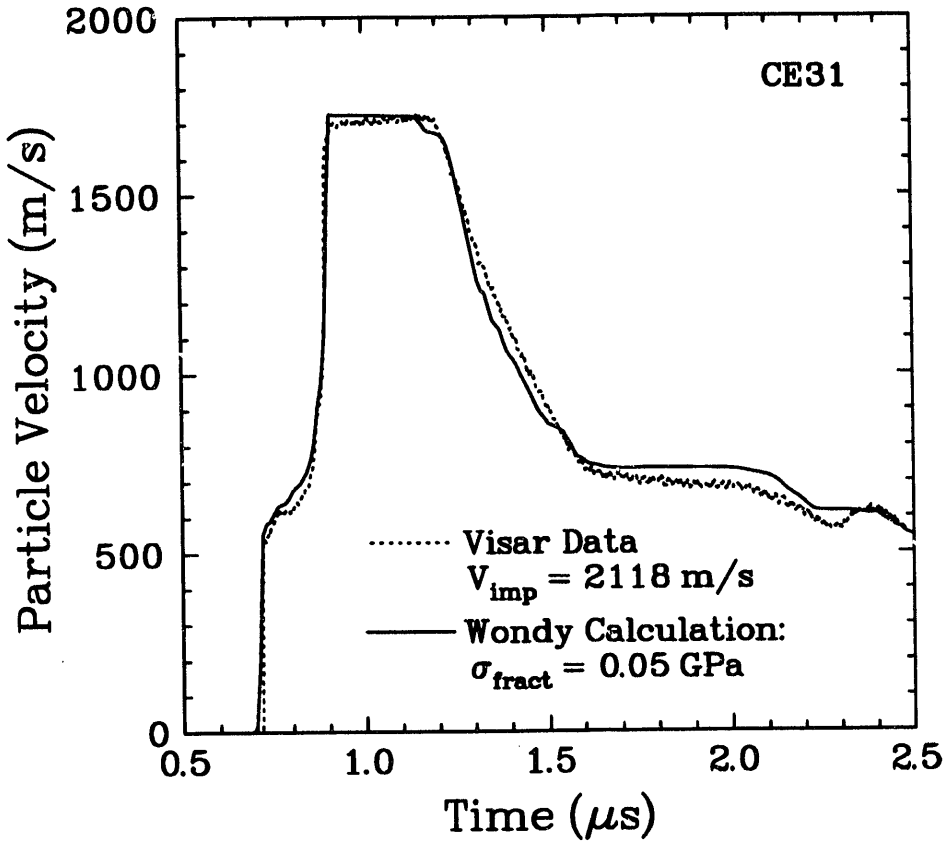

Figure 5. Comparison of VISAR wave profile for test CE-31 and Wondy wave-code solution with strain-hardening elastic-plastic model for silicon carbide.

The corresponding fits to the particle velocity data for the two lower amplitude experiments, CE-4 and CE-5, have been reported by Kipp and Grady (1989). The comparison of calculated and experimental particle velocity histories for the highest amplitude experiment, CE-31, is shown in Figure 5. Note that the calculation captures nearly all of the character of the data, except the initial structure of the release at 1.2 μs, where the effect of the 0.75 GPa yield in the tantalum is too pronounced. This calculation used the same parameters as those reported by Kipp and Grady (1989) for the SiC (cf. Table 3) in a strain-hardening model (6 term fit, with an initial yield of 13.0 GPa; the 6 pairs of the hardening fit are (Y_i GPa, x_i weight) = (13.0,0.307), (14.5,0.231), (16.0,0.152), (17.0,0.076), (19.0,0.115),and (20.0,0.115)) to reproduce the transition from elastic to permanent deformation states (State 4 in WONDY).

Table 3: Material Properties

Material	Reference Density	Sound Speed	Slope	Gruneisen Coefficient	Poisson's Ratio	Initial Yield
	(kg/m^3)	(m/s)				(GPa)
Foam	640	1500	2.0	1.0	~	~
Tantalum	16650	3293	1.307	1.60	0.335	0.75
LiF	2641	5148	1.353	1.50	~	~
SiC	3177	8186	1.0	1.0	0.160	13.0
Al	2758	5328	1.338	2.0	0.333	0.30

In the experiment CE-32, the elastic behavior of the material was examined using SWAP (Barker and Young, 1974), which uses a solution technique based on the x-t characteristics. This code provides for sharp shocks and incremental steps for structured waves. Assuming a linear shock-particle velocity relationship for the Hugoniot, the correct slope of the release wave could be obtained with an S_l of 1.25, but the ultrasonic longitudinal velocity of 12060 m/s for the reference velocity C_l resulted in a pulse width that was too short by about 3%. A reference velocity of C_l = 11700 m/s was required to widen the pulse width sufficiently to agree with the measured pulse width (Figure 6).

The calculated Hugoniot state properties for the four experiments are tabulated in Table 4. When compared to the corresponding entries in Table 2 (Plastic State for CE-4, CE-5, and CE-31, and Elastic State for CE-32), excellent agreement is observed in the two approaches to determine the Hugoniot state values.

Table 4: WONDY Calculations of Hugoniot States

Test Number	Particle Velocity	Density	Specific Volume	Stress	Longitudinal Sound Speed
	(m/s)	(kg/m^3)	(m^3/Mg)	(GPa)	(m/s)
CE-4	771	3412	0.2931	27.85	12923
CE-5	1050	3518	0.2843	36.62	13277
CE-31	1421	3660	0.2732	49.01	13713
CE-32	306	3257	0.3070	12.05	12368

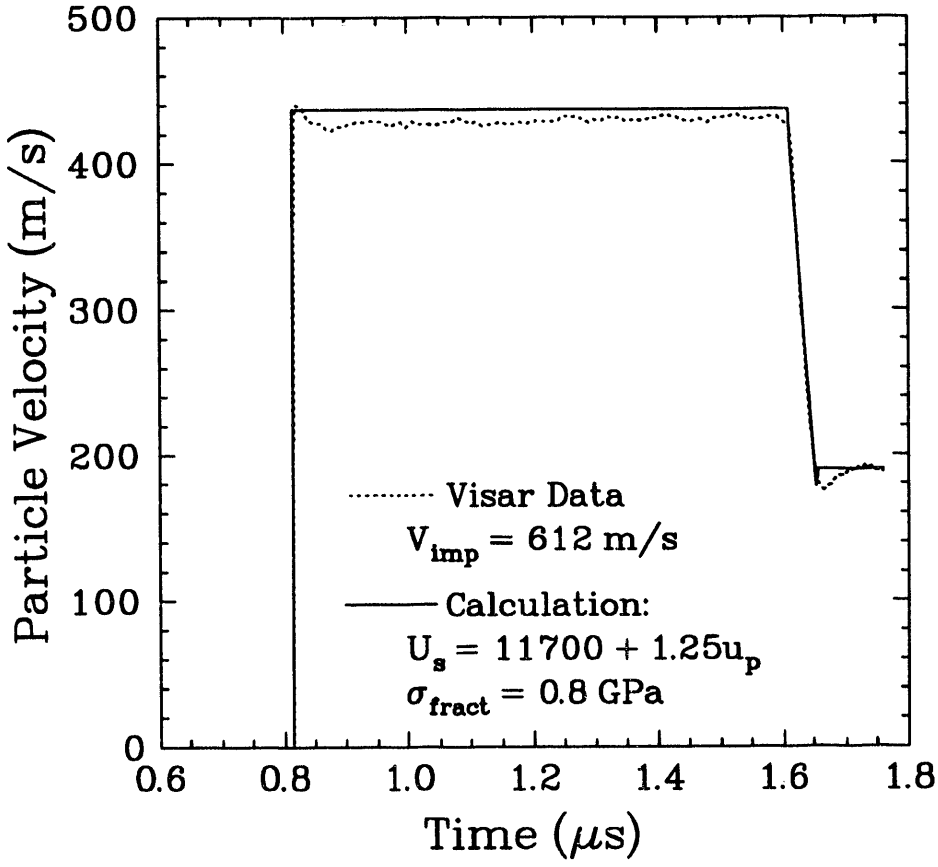

Figure 6. Comparison of VISAR wave profile for test CE-32 and SWAP wave-code solution.

(Intentionally Left Blank)

5. Strength Properties

The Hugoniot elastic limit identifies initial yield in the ceramic and provides an estimate of the initial dynamic material strength. The assumption that the Hugoniot elastic limit accurately characterizes the post-yield shear strength, however, can be seriously in error. Accumulated inelastic deformation along with the changing confining pressure as the Hugoniot state is approached in the plastic wave can markedly alter the strength of the material.

The strength at the Hugoniot state can be determined from the shock-wave data through direct comparison of the longitudinal Hugoniot stress states with the hydrodynamic or mean stress state of the material at the same specific volume. The hydrodynamic properties are usually not well known, however, and are frequently estimated by theoretical extrapolation of ultrasonic data. Nevertheless, the very high strength of the ceramics of interest makes this technique a reasonable method for calculating dynamic strength properties.

Because of the inertially constrained condition of uniaxial strain in the planar impact configuration, ($\varepsilon_x = 1-\rho_o/\rho$, $\varepsilon_y = \varepsilon_z = 0$), the resolved shear stress, $\tau = (\sigma_x - \sigma_y)/2$, within the elastic shock wave increases until the dynamic yield strength of the material is achieved at an average confining pressure, $p = (\sigma_x + 2\sigma_y)/3$. The axial stress at this critical point is identified as the Hugoniot elastic limit, $\sigma_x = \sigma_{hel}$, and the equivalent unconfined yield strength, $Y = 2\tau$ assuming von Mises yield conditions and linear elasticity within the yield surface is,

$$Y = 2\frac{C_s^2}{C_l^2}\sigma_{hel} \ . \tag{1}$$

Hugoniot elastic limit values for Eagle Picher silicon carbide are provided in Table 2. A nominal yield strength calculated for silicon carbide from Equation (1) is $Y = 12.4$ GPa, based on a Hugoniot elastic limit of $\sigma_{hel} = 15.3$ GPa.

Calculation of the post-yield dynamic strength at the Hugoniot state through comparison of the axial stress states measured in the planar impact experiment with the corresponding pressure-volume states is illustrated in Figure 7. The measured axial stress σ_x and the corresponding transverse stress σ_y will relate to the mean pressure curve as shown in Figure 7a. The post-yield resolved shear strength at subsequent Hugoniot states is calculated through comparison of the mean stress and axial stress behavior at the same specific volume through the relation,

$$\tau = \frac{3}{4}(\sigma_x - p) \ . \tag{2}$$

Materials can exhibit different strength behavior with increasing Hugoniot stress (Figure 7b). Ideal plasticity would imply constant strength (constant offset between the

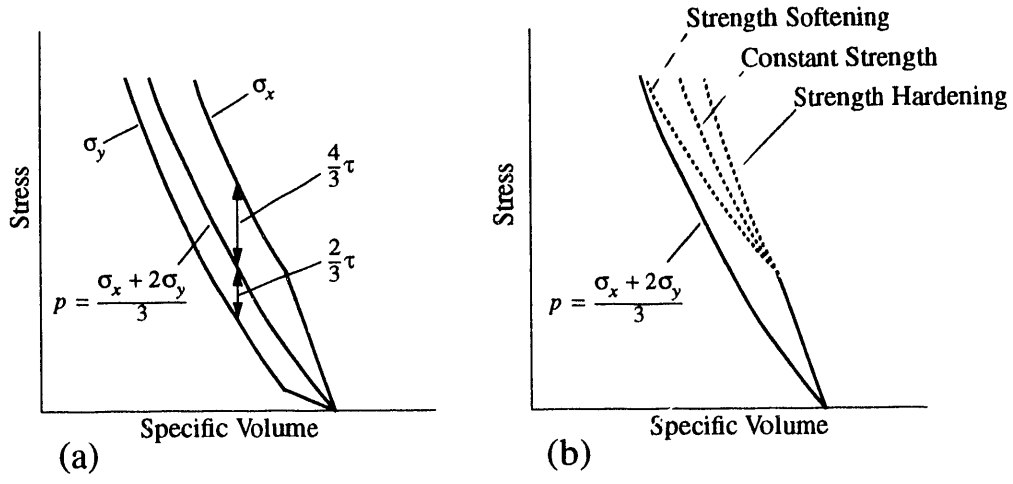

Figure 7. Strength properties of an elastic-plastic material.

mean stress and Hugoniot stress states). Both strength hardening and strength softening on the Hugoniot have also been observed for other ceramics (Kipp and Grady, 1989).

The pressure-volume compression curves for most of the high strength ceramics of interest have not been measured. Quite useful estimates of the hydrodynamic behavior, however, can be established from the reasonably mature understanding of the systematics of solid-state compressibility. Finite strain Burch-Murnaghan, or equivalently, linear shock-velocity versus particle-velocity, representations of material compressibility [Jeanloz, 1989] adequately describe the pressure-volume response of most single phase solids to 20% strains or higher. For the latter representation, two parameters C_o and S_o in a linear shock velocity versus particle velocity relation along with the initial theoretical solid density ρ_o of the material leads to a hydrodynamic pressure versus specific-volume relation for the material,

$$p = \frac{\rho_o C_o^2 \varepsilon}{(1 - S_o \varepsilon)^2}, \tag{3}$$

where the volume strain is $\varepsilon = \varepsilon_x = 1 - \rho_o/\rho$.

The theoretical density is known for the material and C_o can be calculated from the ultrasonic elastic bulk modulus, $C_o = \sqrt{K_o/\rho_o}$. The nonlinearity parameter S_o can be obtained from high pressure Hugoniot data or, alternatively, can be calculated from the relation $S_o = (K_o' + 1)/4$ where $K_o' = dK_o/dp$ is the adiabatic pressure derivative of the bulk modulus. High-pressure Hugoniot data indicate that S_o is close to 1.0 for silicon carbide [Gust, et al, 1973]. Data from Aleksandrov et al (1990) provide $K_o' = 3.9 \pm 0.2$ which yields $S_o \cong 1.2$. Reasonable estimates of the mean stress behavior are compared with Hugoniot states in Figure 4. The two curves assume $S_o = 0.8$ and $S_o = 1.2$, respectively. These results were used to establish the post-yield shear-stress states shown in Figure 8.

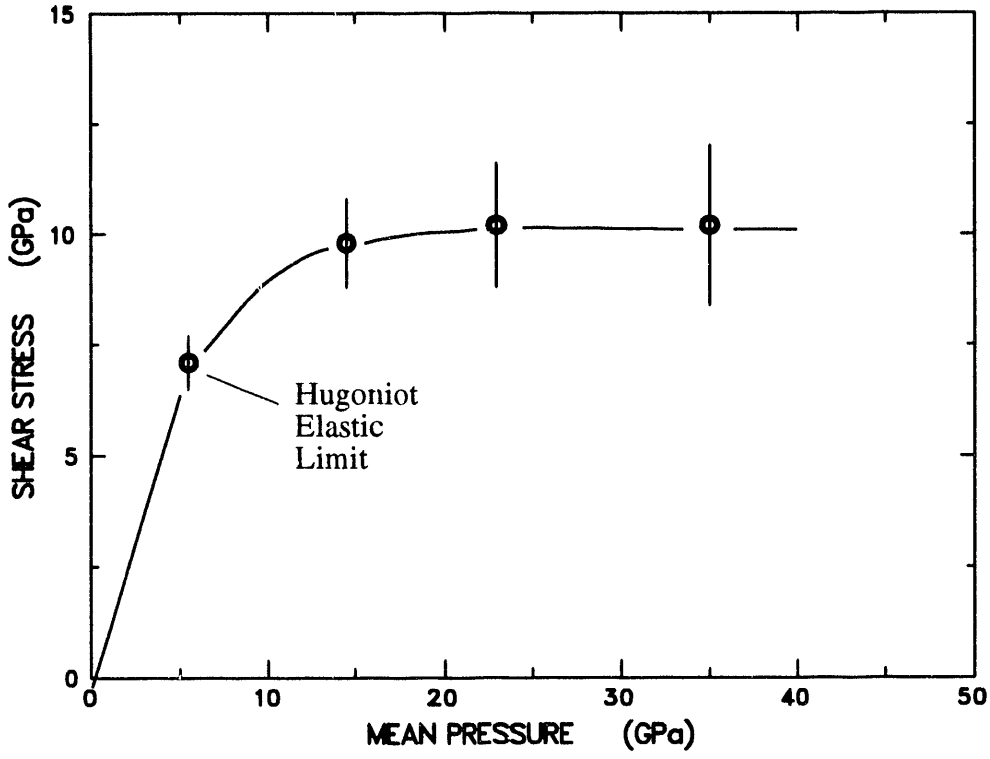

Figure 8. Shear stress at the Hugoniot state inferred from Hugoniot and calculated hydrodynamic curve.

Several material complications can affect the analysis just described. First, impurities which are introduced in the processing of commercial ceramics, if in sufficient quantities, can shift the calculated hydrodynamic curve and must be accounted for. Second, porosity, which exists in virtually all ceramics, must be crushed out before the mean stress curve and the hydrodynamic curve coincide. In general this crush curve is not known. In calculating a shear strength at the Hugoniot state for the three experiments it was assumed that complete pore collapse was achieved and comparison with the theoretical-density hydrodynamic curve was made. The difference between twice the shear strength at the Hugoniot elastic limit (Figure 8) and the dynamic yield calculated from Equation 1 is probably a consequence of porosity complications in the analysis.

In Figure 8 an initial dynamic yield of approximately 7 GPa is observed to harden to about 10 GPa with increasing Hugoniot stress. Uncertainties are larger at higher pressures because of corresponding uncertainties in the mean stress curve. Post-yield stress hardening is also indicated by the ramp character of the measured wave profiles immediately following the elastic precursor wave. Although pressure hardening is commonly used to model the shear-strengthening properties of silicon carbide, inelastic strain or strain-rate hardening cannot be ruled out.

(Intentionally Left Blank)

6. Release Properties

The present planar impact experiments on ceramic materials were designed so that shock compression followed by dynamic decompression and stress release, under controlled uniaxial strain conditions, were achieved. The release portion of the measured wave profile provides dynamic material property data on the cyclic or hysteretic behavior of the stress-loaded ceramic. Release and hystereses properties determine energy absorption and transmission characteristics of material elements and consequently influence the overall penetration stopping resistance of high-strength ceramics. Release-wave dispersion data have been used to infer the confining pressure dependence of shear strength during stress unloading [Chen, 1991] and reverse plasticity properties [Steinberg, 1990]. Further, during high velocity penetration, material compressibility must be correctly modelled. Release-wave measurements provide high-pressure elasticity data needed to properly model finite compressibility.

Release properties of the ceramic were determined from the wave profile data through arrival time and structure of the release wave immediately following the peak plateau in the wave profile (Figure 3). Dispersion (spreading) of the release wave is a consequence of elastic nonlinearity and inelastic deformation characteristics of the material during uniaxial unloading. Both molecular and microstructural properties of the ceramic at high pressure play a role in determining this feature of the wave propagation process.

Extraction of material property data from the release-wave behavior through analytic methods involves difficulties not encountered in the compressive Hugoniot analysis [Grady, 1991]. Assumptions are necessary which are difficult to assess and may or may not be acceptable. Certain material property features such as the nonlinear elastic properties near the shock state can be determined by analytic methods. Other properties are more easily extracted through interactive computer analysis [Kipp and Grady, 1989].

Longitudinal sound velocity C_l and the corresponding longitudinal modulus,

$$K_l = \rho \frac{d\sigma}{d\rho} = \rho C_l^2 , \tag{4}$$

determined from the three experiments involving symmetric silicon carbide impact are plotted in Figure 9. These data were determined from the transit time of the first arrival of the release wave. Eulerian or spatial wave velocities and corresponding moduli are plotted in the Figure. Note that values are several percent lower than those inferred from computational solutions (Table 4). Ultrasonic values for longitudinal velocity and modulus are also shown. The observed discrepancy between ultrasonic data and the shock data extrapolated to zero pressure density is attributed to the percent level porosities in the ceramic samples.

In Figure 10 the stress derivative of the modulus, $K_l' = dK_l/d\sigma$ is plotted. These data were calculated directly from individual profiles by calculating the initial slope of each individual release wave through the expression,

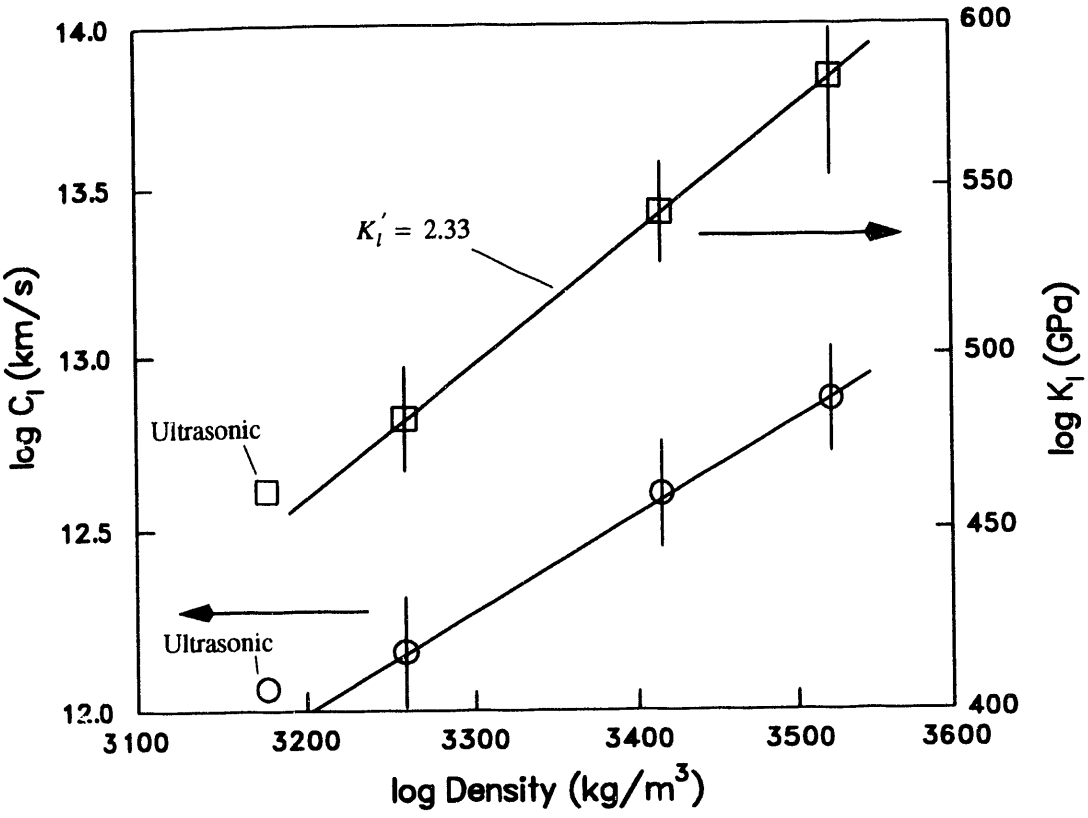

Figure 9. Initial release velocity and longitudinal modulus at the Hugoniot state. Ultrasonic data correspond to points at initial density of 3177 kg/m^3.

$$K_{l*}' = \frac{d}{d\sigma}\rho_o C_{l*}^2 = \rho_o \frac{dC_{l*}^2}{du}\frac{du}{d\sigma} = \rho_o \frac{dC_{l*}^2}{du}\frac{1}{\rho_o C_{l*}} = 2C_{l*}' \quad . \tag{5}$$

The starred properties in Equation 5 correspond to Lagrangian velocities or moduli. Note that both stress and particle-velocity derivatives are implied. The Eulerian modulus was then provided by,

$$K_l' = \frac{\rho_o}{\rho}K_{l*}' - 1 \quad . \tag{6}$$

The data in Figure 10 indicate a decreasing K_l' with increasing density. From the slope of the data in Figure 10 it was determined that $K_l K_l'' = -24.9$. This property compares well in both sign and magnitude with comparable bulk moduli data on alkali halides [Ruoff and Chhabildas, 1979]. It is nearly identical to the very accurate measurement made on NaCl by Chhabildas and Ruoff (1976).

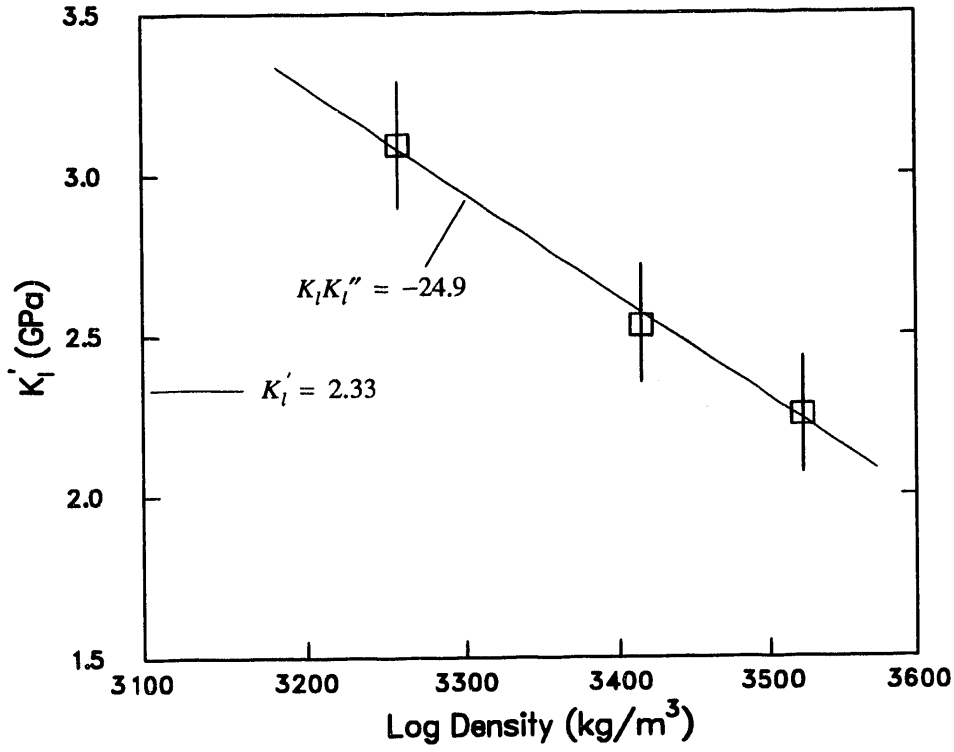

Figure 10. Stress derivative of the release moduli for silicon carbide from initial dispersion of unloading wave.

The stress derivative of the modulus can also be calculated from the data in Figure 9 through,

$$K_l' = \frac{dK_l/d\rho}{K_l/\rho}, \tag{7}$$

A value of $K_l' = 2.33$ was calculated and is in reasonable agreement with the independent data of Figure 10.

It is important to recognize that K_l' determined from the shock data under controlled uniaxial strain conditions is not necessarily equivalent to the pressure derivative of the bulk modulus commonly reported in static high pressure equation-of-state studies. It is equivalent only if Poisson's ratio (or equivalently, the ratio K/G) is independent of the state of mean stress. The nonlinear longitudinal coefficients are governed by the same intermolecular force laws, however, and provide useful data for verifying high-pressure equations of state of ceramic materials.

It is worth noting that the data for K_l' in Figure 10, when extrapolated to the zero pressure theoretical density for silicon carbide of 3210 kg/m^3 yields a zero pressure value of about $K_{lo}' \cong 3.2$. This is somewhat lower than the corresponding value for the pressure dependence of the bulk modulus of $K_{lo}' \cong 3.7 - 4.0$ measured by Aleksandrov, et al. (1990). Ignor-

ing possible differences due to the comparison of dynamic and static data, this result would suggest some sensitivity of Poisson's ratio to compression.

The broader dynamic stress versus strain properties of silicon carbide during stress wave decompression can be determined from the full release profile through a method of interactive computer analysis. This method used the strain-hardening elastic-plastic model discussed in Section 4 with parameters which were adjusted through interactive stress-wave calculations until agreement with arrival and shape of the compression and release wave was achieved. The resulting stress-strain path was then accepted as the material response for that wave profile. The inferred stress-strain paths from computer simulations are compared with Hugoniot and calculated hydrodynamic behavior in Figure 4.

It is important to note the near metal-like elastic-plastic behavior of silicon carbide. The dynamic stress-strain paths in Figure 4 indicate an initial and sustained high-level of shear strength. Unloading behavior is also characteristic of elastic-plastic response.

The release curve in test CE-32 was unique in that the peak stress state achieved prior to unloading was well below (approximately 75%) the Hugoniot elastic limit of the silicon carbide ceramic. Consequently, the release wave should represent strictly nonlinear elastic response of the material. Elastic properties have been determined by Kipp and Grady (1992) and are discussed in Section 4. This release profile also provides a spall pullback signal. A spall strength based on an acoustic approximation is calculated from the relation

$$\sigma_s = \frac{1}{2}(\rho_1 C_1 + \rho_2 C_2)\,\Delta u \quad , \qquad \text{(EQ 8)}$$

where 1 and 2 refer to elastic properties of silicon carbide and lithium fluoride, respectively, and Δu is the amplitude of the velocity pullback signal (see profile for CE-32 in the Appendix). A spall strength of 0.42 GPa was calculated for silicon carbide from the test results of CE-32. Pullback signals characteristic of dynamic tension and spall were not observed in the three tests in which the Hugoniot elastic limit was exceeded during initial shock compression. It can be speculated that pervasive microcracking during inelastic deformation in the compression shock process seriously degraded the cohesive properties of the ceramic.

Finally, test CE-42 was performed in which the layered-material impactor led to a history of cyclic loading in which the silicon-carbide ceramic was first shock compressed to approximately 30 GPa (nearly identical to test CE-4) and then decompressed to about one-half of the Hugoniot stress. This decompression is a backward-facing release wave originating at the lithium-fluoride-window interface and, consequently, is not observed in the interface velocity profile shown in Figure 11. A tantalum plate behind the lithium fluoride in the layered impactor leads to recompression and a subsequent second decompression of the silicon carbide. The elastic-plastic character on recompression is observed in the second wave in Figure 11 at about 1.5-1.6 μs. This experiment provides a stringent test for computational material response models in terms of cyclic shear-strength behavior.

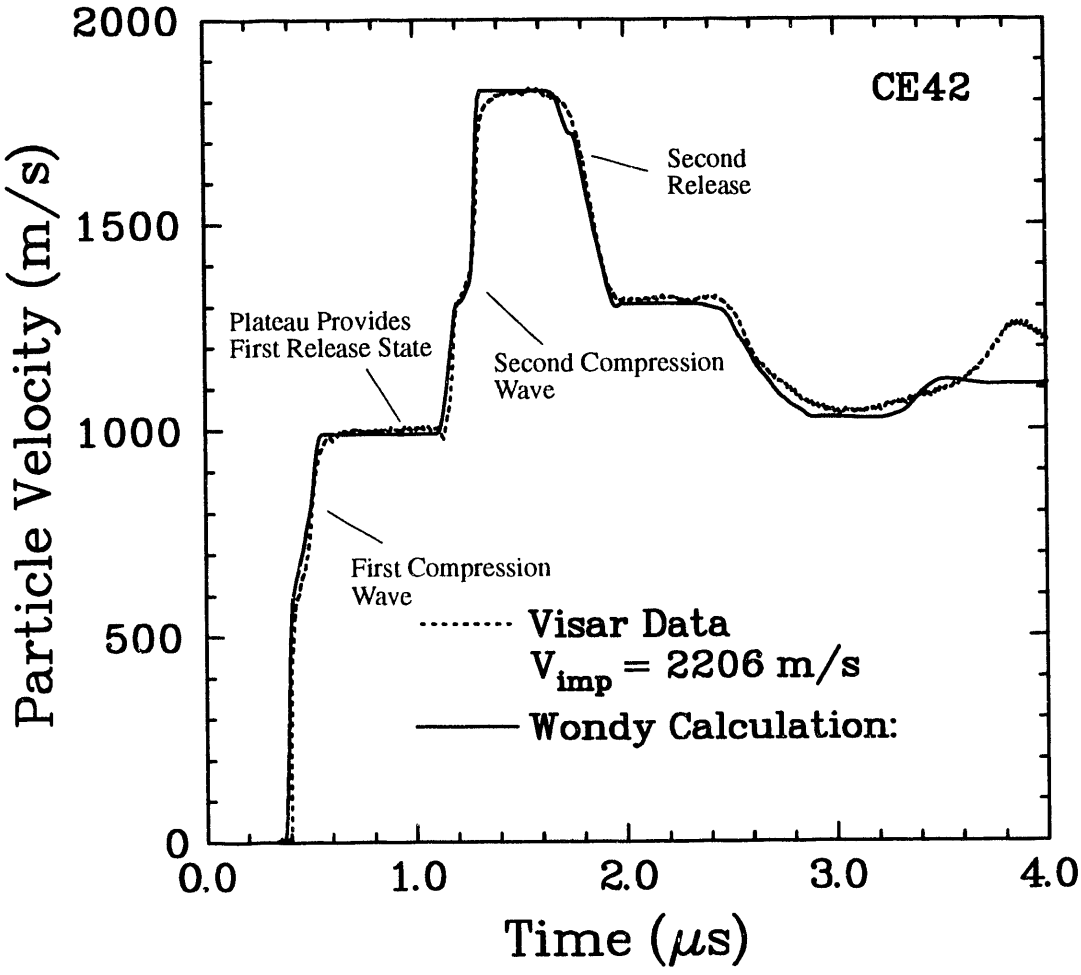

Figure 11. Multiple shock compression and release experiment and calculation in silicon carbide.

A WONDY calculation of experiment CE-42 was made using the strain-hardening elastic-plastic parameters for the silicon carbide and the ancillary material parameters listed in Table 3. The comparison is shown in Figure 11 in which excellent agreement is observed for nearly all of the wave structure features between calculation and experiment. The exceptions are the absence of the slight down turn at the end of the first shock, the dispersed wave structure at the top of the second shock, and the exaggerated release in the tantalum at the end of the second shock.

In all other respects, the timing of waves and the breaks for yielding within the profile are reproduced quite accurately by the calculation. For this silicon carbide, the strain-hardening elastic-plastic model is able to represent the material response over a wide range of shock load and release under conditions of uniaxial strain deformation.

(Intentionally Left Blank)

Conclusions

From the shock response characteristics of silicon carbide measured in the present investigation, the material appears to be very metal-like in its dynamic shear properties. Although the dynamic shear strength of silicon carbide ceramic is an order of magnitude higher than some of the strongest metals, its hardening characteristics during shock compression, and its elastic-plastic-like behavior upon deformation reversal during shock release, are very similar to the behavior of a number of metals. A work-hardening elastic-plastic model was quite adequate for numerical simulation of the measured wave-profile data. The same cannot be said for other ceramics which have been tested [Kipp and Grady, 1989].

The present analysis indicates a hardening of the shear strength of silicon carbide during post-yield deformation by as much as 30 to 50 percent above the initial yield value at the Hugoniot elastic limit. This calculation is based on the offset between the measured Hugoniot data and a calculated hydrodynamic curve. Diamond-anvil measurements by Bassett and Weathers [Holmquist, 1991] indicate somewhat stiffer hydrostatic behavior for silicon carbide. Recent hydrodynamic shock-compression experiments on silicon carbide and metal mixtures, however, indicate a compressibility for silicon carbide closer to the calculated extrapolation of ultrasonic data [Grady, 1992]. Thus, although some degree of post-shock hardening appears to be appropriate for silicon carbide, more detailed statements will have to wait until the hydrodynamic response issue is resolved.

An extensive study of the spall strength of silicon carbide has not yet been performed. However, in one experiment in which shock compression to about 75% of the Hugoniot elastic limit was achieved, a spall strength of about 0.4 GPa was estab;ished for the material— comparable with other high-strength ceramics (Al_2O_3, B_4C, TiB_2, AlN). Further, the shape of the spall signal and the low value of impulse coupled into the spalled segment suggested a very brittle dynamic fracture process. Experiments performed at shock stresses above the Hugoniot elastic limit show negligible spall strength — consistent with loss of material cohesion during compressive shock deformation. These observations are similar to those of Munson and Lawrence (1979) on aluminum oxide ceramic in which they attributed loss of tensile strength to pervasive microcracking during shock compression. Similar mechanisms appear to govern deformation in silicon carbide.

Gust, et al. (1973) have suggested a shock-induced phase change in silicon carbide at about 24 GPa from shock-compression data. The present shock-wave data do not provide clear evidence for a phase transition within the 0 to 50 GPa shock-pressure range of the study. Examination of silicon carbide samples shocked to as high as 80 GPa [Kovtun and Timofeeva, 1988] did not reveal quenched high-pressure phases. Also, the static compression study of Bassett and Weathers [Holmquist, 1991] on silicon carbide does not provide evidence for a high-pressure transition in static high-pressure measurements.

(Intentionally Left Blank)

References

1. Aleksandrov, I.V., A. F. Goncharov, E. V. Jakovenko and S. M. Stishov, *High Pressure Research - XII AIRAPT Conference*, Gordon and Breach Science Pub., pp. 938-940, 1990.

2. Barker, L. M. and R. E. Hollenbach, J. Appl. Phys., 43, 4669, 1972.

3. Barker, L. M. and E. G. Young, Sandia National Laboratories Report SLA-74-0009, June 1994.

4. Chen, P. J., (private communication), 1991.

5. Chhabildas, L. C. and A. L. Ruoff, J. Appl. Phys., 47, 4182-4187, 1976.

6. Grady, D. E., *Proceedings of the XIII International AIRAPT Conference*, Bangalore, India, October 7-11, 1991 (in press).

7. Grady, D. E., Sandia National Laboratories Technical Memorandum (unpublished), June, 1992.

8. Gust, W. H.. A. C. Holt, and E. B. Royce, J. Appl. Phys., 44, 550, 1973.

9. Holmquist, T. J., Alliant Techsystem Report, October 1991.

10. Kipp, M. E. and R. J. Lawrence, Sandia National Laboratories Technical Report SAND81-0930, June 1982.

11. Kipp, M. E. and D. E. Grady, Sandia National Laboratories Technical Report SAND89-1461, July 1989.

12. Kipp, M. E. and D. E. Grady, *Shock Waves in Condensed Matter - 1991*, S. C. Schmidt, et al., eds., North Holland, pp. 459-462, 1992.

13. Kovtun, V. I., and I. I. Timofeeva, Sov. Powder Metall. Metal Ceram., 8/308(1988),673.

14. Jeanloz, R., J. Geophys. Res., 94, 5873-5886, 1989.

15. Munson, D. E. and R. J. Lawrence, J. Appl. Phys., 50, 6272, 1979.

16. Ruoff, A. L., and L. C. Chhabildas, *High-Pressure Science and Technology - XI AIRAPT Conference, Volume 1*, K. D. Timmerhaus and M. S. Barber, eds., Plenum Press, pp. 19-32, 1979.

17. Steinberg, D. J., Lawrence Livermore National Laboratory Technical Report UCRL-ID-106004, September, 1990.

18. Wise, J. L. and L. C. Chhabildas, *Shock Waves in Condensed Matter - 1985*, edited by Y. M. Gupta (Plenum, 1986) p. 441.

APPENDIX A

Interface wave-profile data

The present appendix is comprised of the primary data sheet for each experimental test including initial material properties, geometry parameters, and the VISAR velocity profile.

TEST NUMBER: CE 4.

TEST PURPOSE: Shock and release equation of state on silicon carbide

TARGET MATERIAL SPECIFICS: Silicon carbide. Density = 3177 kg/m3. CL = 12.06 km/s. CS = 7.67 km/s. Sample (disc) thickness = 8.939 mm. Sample diameter = 55.0 mm.

PROJECTILE MATERIAL SPECIFICS: Symmetric impact (SiC-on-SiC). Sample (disc) thickness = 3.987 mm. Sample diameter = 55.0 mm. Impactor backing = polyurathane foam -- density = 320 kg/m3 -- thickness = 6 mm.

WINDOW MATERIAL SPECIFICS: Lithium fluoride (cylinder). length = 25.4 mm. Diameter = 50.8 mm.

IMPACT VELOCITY: 1.542 km/s.

IMPACT TIMING: First wave arrival corresponds to ultrasonic longitudinal transit time through sample.

COMMENTS: Samples were produced by Eagle Picher Industries and provided by Los Alamos National Laboratories.

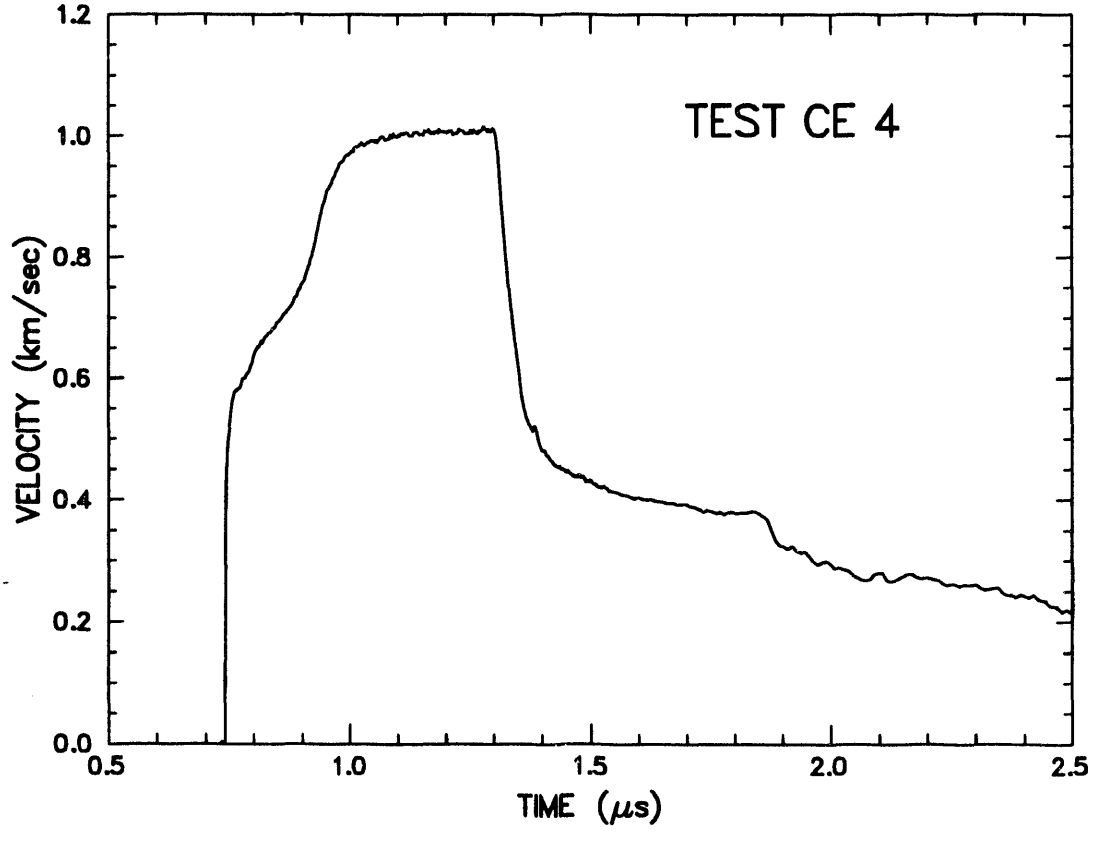

TEST NUMBER: CE 5.

TEST PURPOSE: Shock and release equation of state on silicon carbide

TARGET MATERIAL SPECIFICS: Silicon carbide. Density = 3177 kg/m3. CL = 12.06 km/s. CS = 7.67 km/s. Sample (disc) thickness = 8.940 mm. Sample diameter = 55.0 mm.

PROJECTILE MATERIAL SPECIFICS: Symmetric impact (SiC-on-SiC).Sample (disc) thickness = 3.995 mm. Sample diameter = 55.0 mm. Impactor backing = polyurathane foam -- density = 640 kg/m3 -- thickness = 6 mm.

WINDOW MATERIAL SPECIFICS: Lithium fluoride (cylinder). length = 25.4 mm. Diameter = 50.8 mm.

IMPACT VELOCITY: 2.100 km/s.

IMPACT TIMING: First wave arrival corresponds to ultrasonic longitudinal transit time through sample.

COMMENTS: Samples were produced by Eagle Picher Industries and provided by Los Alamos National Laboratories.

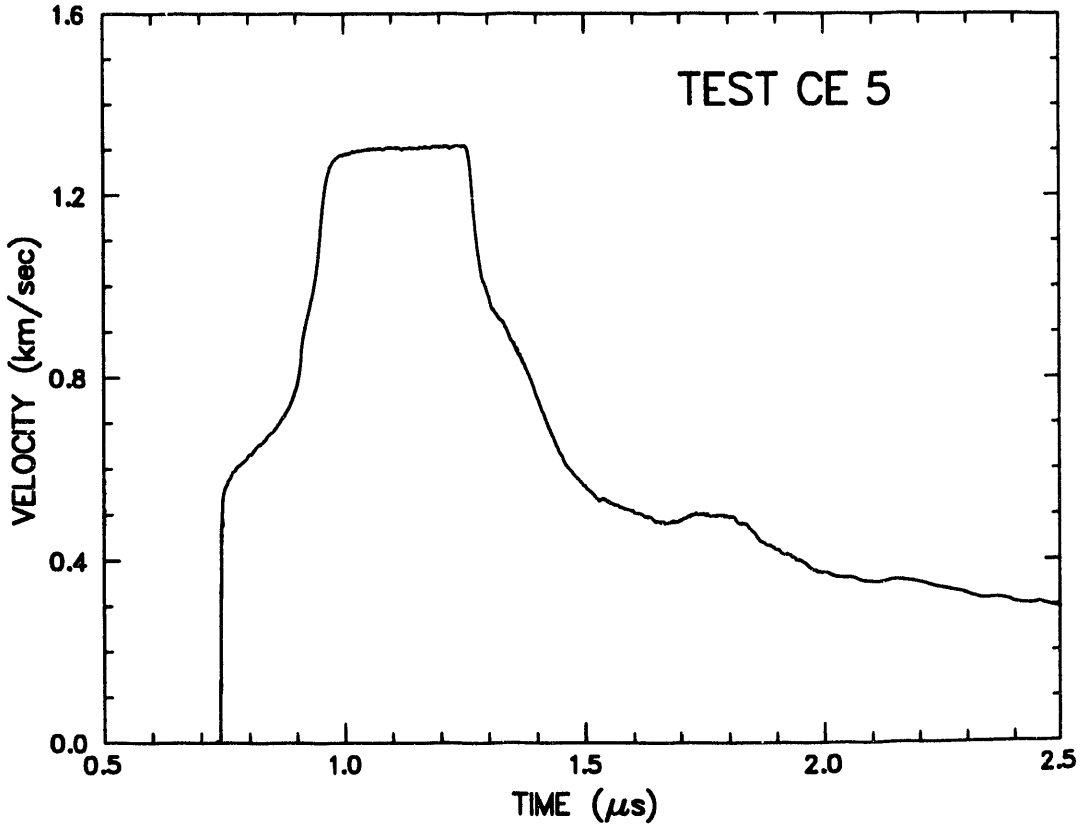

TEST NUMBER: CE 31.

TEST PURPOSE: Shock and release equation of state on silicon carbide

TARGET MATERIAL SPECIFICS: Silicon carbide. Density = 3177 kg/m3. CL = 12.06 km/s. CS = 7.67 km/s. Sample (disc) thickness = 8.956 mm. Sample diameter = 52.5 mm.

PROJECTILE MATERIAL SPECIFICS: Tantalum impactor. Sample (disc) thickness = 1.515 mm. Sample diameter = 87.5 mm. Impactor backing = polyurathane foam -- density = 640 kg/m3 -- thickness = 6 mm.

WINDOW MATERIAL SPECIFICS: Lithium fluoride (cylinder). length = 25.4 mm. Diameter = 50.8 mm.

IMPACT VELOCITY: 2.118 km/s.

IMPACT TIMING: First wave arrival corresponds to ultrasonic longitudinal transit time through sample.

COMMENTS: Samples were produced by Eagle Picher Industries and provided by Los Alamos National Laboratories.

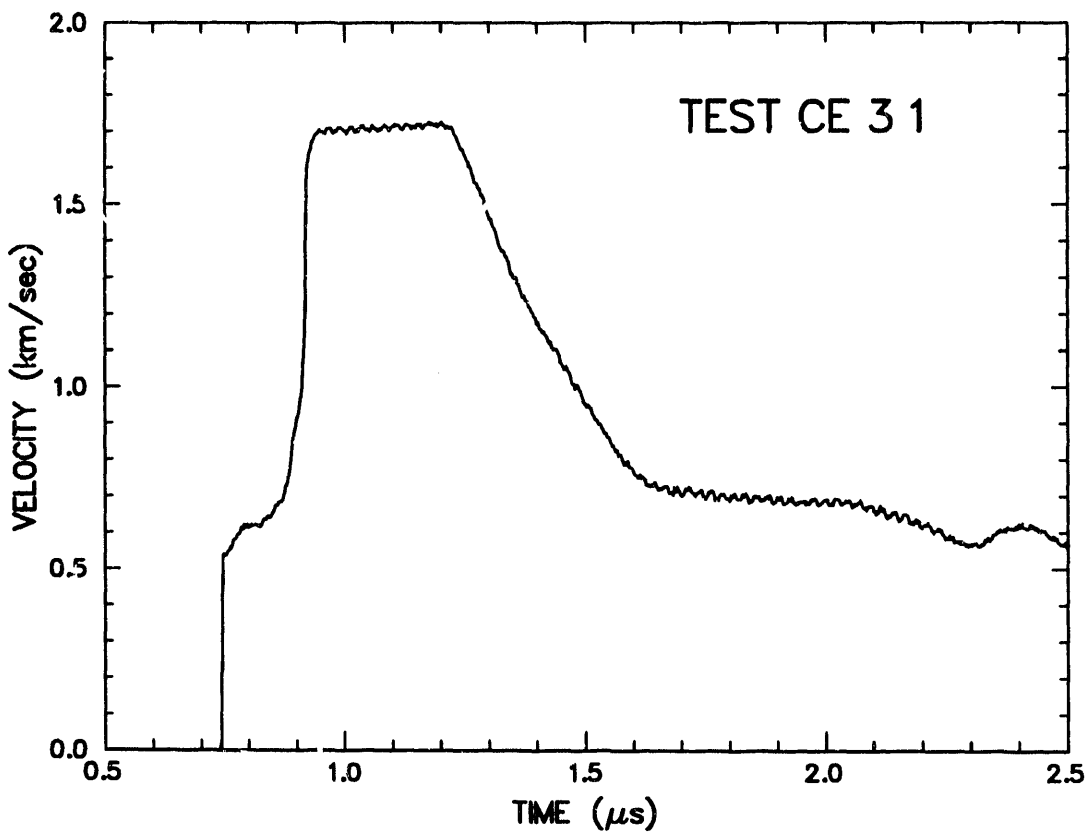

TEST NUMBER: CE 32.

TEST PURPOSE: Elastic nonlinearity and spall on silicon carbide

TARGET MATERIAL SPECIFICS: Silicon carbide. Density = 3177 kg/m3. CL = 12.06 km/s. CS = 7.67 km/s. Sample (disc) thickness = 9.841 mm. Sample diameter = 50.0 mm.

PROJECTILE MATERIAL SPECIFICS: Symmetric impact (SiC-on-SiC). Sample (disc) thickness = 4.958 mm. Sample diameter = 50.0 mm. Impactor backing = polyurathane foam -- density = 320 kg/m3 -- thickness = 6 mm.

WINDOW MATERIAL SPECIFICS: Lithium fluoride (cylinder). length = 25.4 mm. Diameter = 50.8 mm.

IMPACT VELOCITY: 0.612 km/s.

IMPACT TIMING: First wave arrival corresponds to ultrasonic longitudinal transit time through sample.

COMMENTS: Samples were produced by Eagle Picher Industries and provided by Los Alamos National Laboratories.

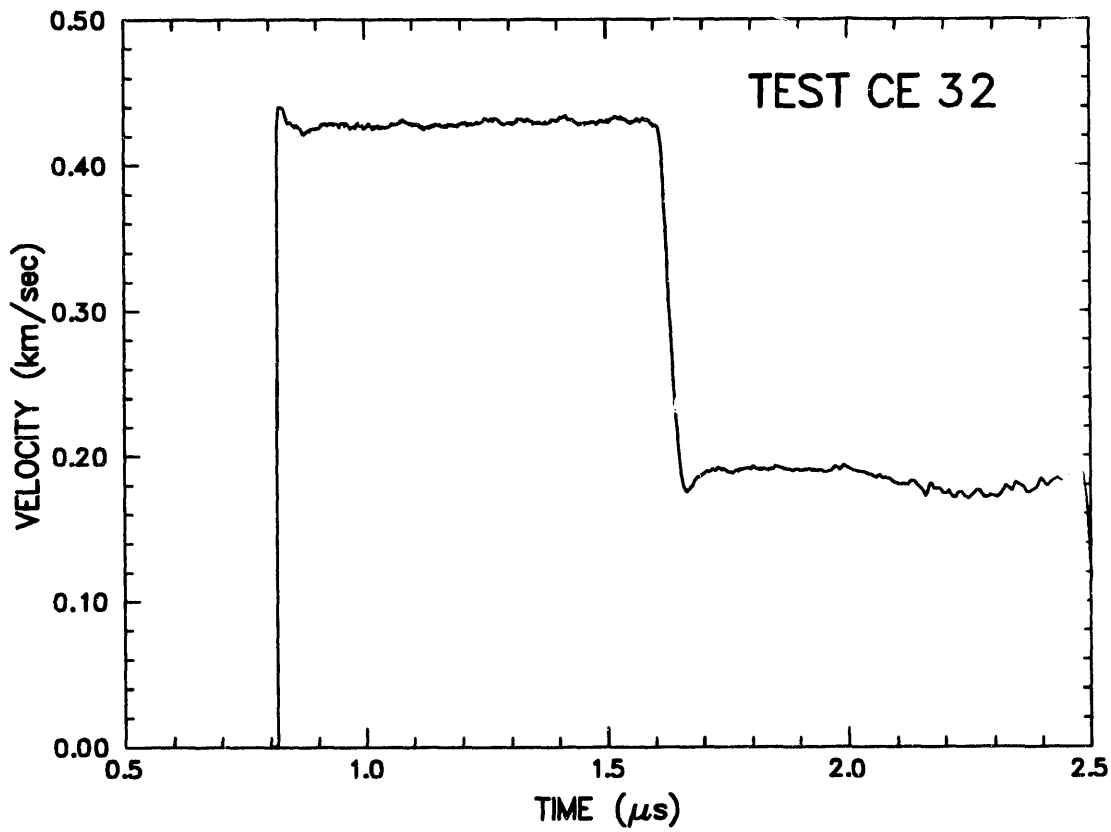

TEST NUMBER: CE 42.

TEST PURPOSE: Multiple shock and release equation of state of silicon carbide.

TARGET MATERIAL SPECIFICS: Silicon carbide. Density = 3177 kg/m3. CL = 12.06 km/s. CS = 7.67 km/s. Sample (disc) thickness = 4.963 mm. Sample diameter = 76.14 mm.

PROJECTILE MATERIAL SPECIFICS: Lithium fluoride impactor. Sample (disc) thickness = 3.297 mm. Sample diameter = 50.8 mm. Lithium fluoride backing = tantalum. Tantalum disc thickness = 1.510 mm and diameter = 87.49 mm. Tantalum disc backed by approximately 12 mm thickness aluminum plate.

WINDOW MATERIAL SPECIFICS: Lithium fluoride (cylinder). length = 25.4 mm. Diameter = 50.7 mm.

IMPACT VELOCITY: 2.206 km/s.

IMPACT TIMING: Profile is not time aligned.

COMMENTS: Samples were produced by Eagle Picher Industries and provided by Los Alamos National Laboratories.

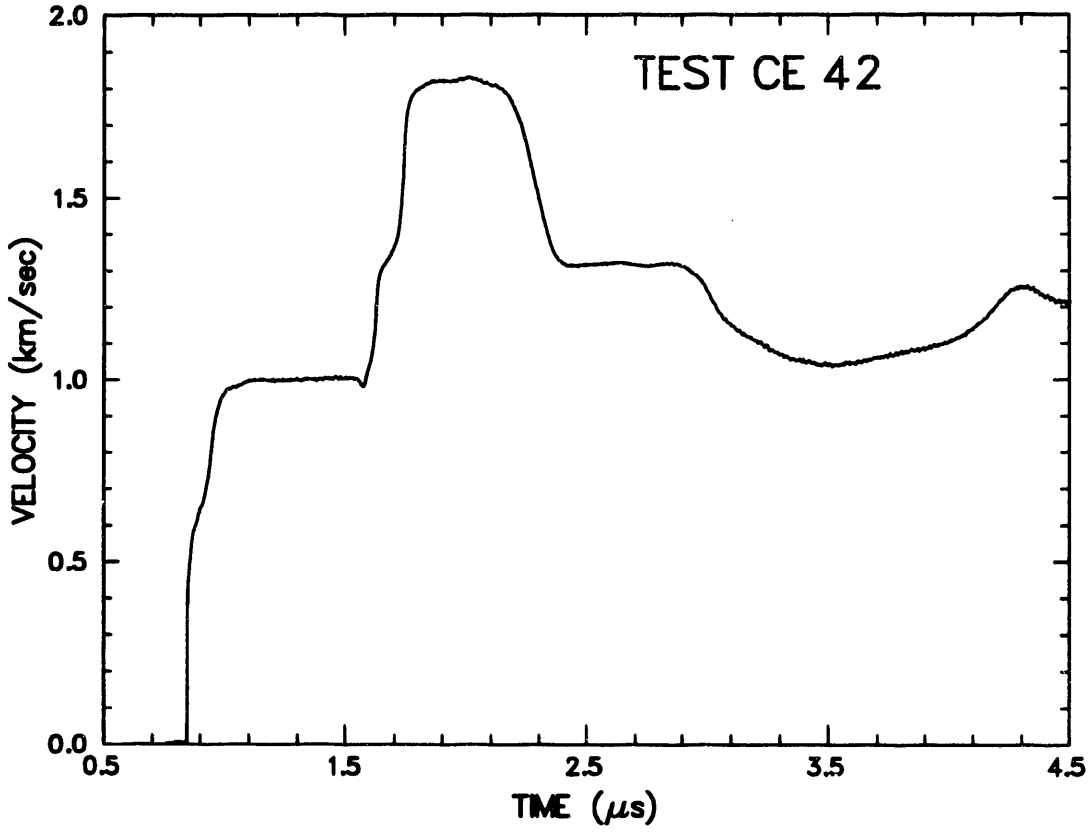

DISTRIBUTION:

INTERNAL

1400 E. H. Barsis
1431 J. M. McGlaun
1431 K. G. Budge
1431 E. S. Hertel
1431 R. J. Lawrence
1431 J. S. Peery
1431 A. C. Robinson
1431 T. G. Trucano
1431 M. K. Wong
1432 P. Yarrington
1432 P. J. Chen
1432 H. E. Fang
1432 A. V. Farnsworth
1432 G. I. Kerley
1432 M. E. Kipp (15)
1432 S. A. Silling
1432 P. A. Taylor
1433 P. L. Stanton
1433 J. A. Ang
1433 L. C. Chhabildas
1433 D. A. Crawford
1433 M. D. Furnish
1433 D. E. Grady (25)
1500 D. J. McCloskey
1511 J. S. Rottler
1512 A. C. Ratzel
1561 H. S. Morgan
1562 R. K. Thomas
1562 J. W. Swegle
2565 S. T. Montgomery1433
6111 J. L. Wise
7141 Technical Library (5)
7151 Technical Publications
7613 Document Processing for DOE/OSTI (2)
8523-2 Central Technical Files
9722 W. Tucker
9723 M. J. Forrestal
9723 V. K. Luk

EXTERNAL

T. F. Adams
Los Alamos National Laboratory
MS F663
Los Alamos, NM 87545

T. J. Ahrens
Geophysics Division MS/252-21
California Institute of Technology
Pasadena, CA 91125

F. Allahdadi
Phillips Laboratory
PL/WSSD
Kirtland AFB, NM 87117-6008

M. L. Alme
102 Stevens Forrest Professional Center
9650 Santiago Road
Columbia, MD 21045

C. E. Anderson
Southwest Research Institute
6220 Culebra Road
San Antonio, TX 78284

D. W. Baum
Lawrence Livermore National Laboratory
Livermore,CA 94550

S. J. Bless
Institute for Advanced Technology
4030-2 W. Braker Lane
Austin, TX 78759-5329

W. Blumenthal
Los Alamos National Laboratory
MS E546
Los Alamos, NM 87545

S. Brar
Impact Physics Laboratory
University of Dayton Research Institute
300 College Park
Dayton, OH 45469-3546

W. J. Bruchey
U.S. Army Research Laboratory
SLCBR-TB-A
Aberdeen Proving Ground, MD 21005-5066

M. Burkett
Los Alamos National Laboratory
MS J576
Los Alamos, NM 87545

A. Charters
General Research Corporation
5383 Hollister Avenue
Santa Barbara, CA 93160-6770

S. Chou
Army Research Laboratory
Materials Directorate
AMSRL-MA-DA
Watertown, MA 02172-0001

R. Clifton
Brown University
Division of Engineering
Providence, RI 02912

J. A. Collins
US Air Force Armament Laboratory
AD/MNW
Eglin Air Force Base, FL 32542-5434

J. W. Coltman
Simula Inc.
10016 South 51st Street
Phoenix, AZ 85044

E. Cort
Los Alamos National Laboratory
MS K574
Los Alamos, NM 87545

D. Curran
SRI International
333 Ravenswood Avenue
Menlo Park, CA 94025

D. Dandekar
U.S. Army Research Laboratory
Materials Directorate
AMSRL-MA-DA
Watertown, MA 02172-0001

K. Epstein
DOW Chemical USA
Ordnance Systems, 800 Building
Midland, MI 48667

P. Follansbee
Los Alamos National Laboratory
MS K663
Los Alamos, NM 87545

J. C. Foster, Jr.
US Air Force Armament Laboratory
AD/MNW
Eglin Air Force Base, FL 32542-5434

J. R. Furlong
SAIC
1710 Goodridge Dr.
McLean VA 22102

Y. Gupta
Washington State University
Department of Physics
Pullman, WA 99163

G. Hauver
U.S. Army Research Laboratory
AMSRL-WT-TA
Aberdeen Proving Ground, MD 21005-5066

T. Holmquist
Alliant Techsystems, Inc.
7225 Northland Drive
Brooklyn Park, MN 55428

Y. Horie
North Carolina State University
Dept. of Civil Engineering
Raleigh, NC 27607

K. Iyer
US Army Research Office
P. O. Box 12211
Research Triangle Park, NC 27709

G. Johnson
Alliant Techsystems, Inc.
7225 Northland Drive
Brooklyn Park, MN 55428

J. N. Johnson
Los Alamos National Laboratory
MS B221
Los Alamos, NM 87545

K. Kimsey
U.S. Army Research Laboratory
Attn: SLCBR-TB-P
Aberdeen Proving Ground, MD 21005-5066

R. W. Kocher
Defense Advanced Research Projects Agency
Land Systems Office
3701 North Fairfax Drive
Arlington, VA 22203-1714

J. Lankford
Southwest Research Institute
6220 Culebra Road
San Antonio, TX 78284

K. T. Leighton
Lanxide Armor Products, Inc.
1300 Marrows Road
P. O. Box 6077
Newark, DE 19714-6077

D. Mandell
Los Alamos National Laboratory
MS F663
Los Alamos, NM 87545

M. Manghnani
Mineral Physics Group
University of Hawaii
2525 Correa Rd.
Honolulu, HA 96822

P. Maudlin
Los Alamos National Laboratory
MS K557
Los Alamos, NM 87545

H. C. Meyer
U.S. Army Research Laboratory
AMSRL-WT-TA
Aberdeen Proving Ground, MD 21005-5066

M. Meyer
Univ. of Calif. at San Diego
Dept. of Applied Mech. & Eng. Sciences
La Jolla, CA 92093

J. D. Morrow
FMC Corporation
Ground Systems Division
1107 Coleman Avenue Box 367
San Jose, CA 95103

S. Nemat-Nasser
Univ. of Calif. at San Diego
Dept. of Applied Mech. & Eng. Sciences
La Jolla, CA 92093

T. Nicholas
Air Force Wright Aeronautical Labs.
Air Force Systems Command
Materials Laboratory
Wright-Patterson AFB, OH 45433

D. Orphal
California Research and Technology, Inc.
5117 Johnson Drive
Pleasanton, CA 94566

R. Palicka
CERCOM, Inc.
1960 Watson Way
P. O. Box 70
Vista, CA 92083

R. Paricio
Coors Ceramics Company
600 Ninth Street
Golden, CO 80401

W. W. Predebon
College ofEngineering
Michigan Technological University
Houghton, MI 49931

G. F. Raiser
Washington State University
Department of Physics
Pullman, WA 99163

A. M. Rajendran
Army Research Laboratory
Materials Directorate
AMSRL-MA-DA
Watertown, MA 02172-0001

G. Randers-Pehrson
US Army Ballistic Research Laboratory
SLCBR-TB-W
Aberdeen Proving Ground, MD 21005-5066

M. Scheidler
U.S. Army Research Laboratory
AMSRL-WT-TD
Aberdeen Proving Ground, MD 21005-5066

P. N. Schneidewind
California Research and Technology, Inc.
5117 Johnson Drive
Pleasanton, CA 94566

S. Segletes
U.S. Army Research Laboratory
SLCBR-TB-W
Aberdeen Proving Ground, MD 21005-5066

D. A. Shockey
Poulter Laboratory
SRI International
333 Ravenswood Avenue
Menlo Park, CA 94025

R. Skaggs
Los Alamos National Laboratory
MS K574
Los Alamos, NM 87545

M. Slavin
U.S. Army Research Laboratory
SLCMT-MCC
Arsenal Street
Watertown, MA 02172-0001

J. M. Staehler
College of Engineering
Michigan Technological University
Houghton, MI 49931

D. Steinberg, MS L35
Lawrence Livermore National Laboratory
P. O. Box 808
Livermore, CA 94550

J. Sternberg
Naval Postgraduate School
Superintendent Code 412B
Monterey, CA 93943

D. J. Viechniki
U.S. Army Research Laboratory
SLCMT-MCC
Arsenal Street
Watertown, MA 02172-0001

T. Wright
U.S. Army Research Laboratory
SLCBR-TB-W
Aberdeen Proving Ground, MD 21005-
5066

DATE
FILMED
10/13/93
END